Thermally activated vapor bubble nucleation: The Landau-Lifshitz–Van der Waals approach

Mirko Gallo, Francesco Magaletti, and Carlo Massimo Casciola*
Department of Mechanical and Aerospace Engineering, Sapienza Università di Roma, Rome, Italy

(Received 13 October 2017; revised manuscript received 16 December 2017; published 22 May 2018)

Vapor bubbles are formed in liquids by two mechanisms: evaporation (temperature above the boiling threshold) and cavitation (pressure below the vapor pressure). The liquid resists in these metastable (overheating and tensile, respectively) states for a long time since bubble nucleation is an activated process that needs to surmount the free energy barrier separating the liquid and the vapor states. The bubble nucleation rate is difficult to assess and, typically, only for extremely small systems treated at an atomistic level of detail. In this work a powerful approach, based on a continuum diffuse interface modeling of the two-phase fluid embedded with thermal fluctuations (fluctuating hydrodynamics), is exploited to study the nucleation process in homogeneous conditions, evaluating the bubble nucleation rates and following the long-term dynamics of the metastable system, up to the bubble coalescence and expansion stages. In comparison with more classical approaches, this methodology allows us on the one hand to deal with much larger systems observed for a much longer time than possible with even the most advanced atomistic models. On the other, it extends continuum formulations to thermally activated processes, impossible to deal with in a purely determinist setting.

DOI: 10.1103/PhysRevFluids.3.053604

I. INTRODUCTION

Thermal fluctuations play a dominant role in the dynamics of fluid systems below the micrometer scale. Their effects are significant in, e.g., the smallest microfluidic devices [1,2] or in biological systems such as lipid membranes [3], for Brownian engines, and in artificial molecular motors [4]. They are crucial for thermally activated processes such as nucleation, the precursor of the phase change in metastable systems. Nucleation is directly connected to the phenomenon of bubble cavitation [5] and of freezing rain [6], to cite a few. There thermal fluctuations allow to overcome the energy barriers for phase transitions [7–9]. Depending on the thermodynamic conditions, the nucleation time may be exceedingly long, the so-called "rare-event"issue. Classical nucleation theory (CNT) [10] provides the basic understanding of the phenomenon, which is nowadays addressed through more sophisticated models like density functional theory (DFT) [11,12] or by means of molecular dynamics (MD) simulations [13]. These approaches need to be coupled to specialized techniques for rare events, like the string method [14], the forward flux sampling [15], and the transition path sampling [16], to reliably evaluate the nucleation barrier and determine the transition

*carlomassimo.casciola@uniroma1.it; http://flumacs.site.uniroma1.it

Published by the American Physical Society under the terms of the Creative Commons Attribution 4.0 International license. Further distribution of this work must maintain attribution to the author(s) and the published article's title, journal citation, and DOI.

path [17]. For many real systems they are often computationally too expensive and therefore limited to very small domains.

Here we adopt a mesoscopic continuum approach, embedding stochastic fluctuations, for the numerical simulation of thermally activated bubble nucleation. Since the pioneering work of Landau and Lifshitz [18] several works contributed to the growing field of "fluctuating hydrodynamics" (FH) [19]. More recently the theoretical effort has been followed by a flourishing of highly specialized numerical methods for the treatment of the stochastic contributions [20–23]. The present model is based on a diffuse interface [24] description of the two-phase vapor-liquid system [25] similar to the one recently exploited by Chaudhri *et al.* [26] to address the spinodal decomposition. The thermodynamic range of applicability of this approach is subjected to some restrictions: (1) at the very first stage of nucleation the vapor nuclei, smaller than the critical size, need to be numerically resolved; analogously, (2) the thin liquid-vapor interface needs to be captured for the correct evaluation of the capillary stresses; and (3) fluctuating hydrodynamics predicts that the fluctuation intensity grows with the inverse cell volume, ΔV, leading to intense fluctuations, contrary to the assumption of weak noise needed to derive the model ($\sqrt{\langle \delta f^2 \rangle}/\langle f \rangle \ll 1$). Notwithstanding these restrictions, where it can be applied, this mesoscale approach offers a good level of accuracy (as will be shown when discussing the results) at a very cheap computational cost compared to other techniques. The typical size of the system we simulate on a small computational cluster ($200 \times 200 \times 200$, nm^3, corresponding to a system of order 10^8 atomistic particles) is comparable with one of the largest MD simulations [27] on a tier-0 machine. Moreover the simulated time is here $T_{\max} \sim \mu$s to be compared with the MD $T_{\max} \sim$ ns. The enormous difference between the two time extensions allows us to address the simultaneous nucleation of several vapor bubbles, their expansion, coalescence, and, at variance with most of the available methods dealing with quasistatic conditions, the resulting excitation of the macroscopic velocity field.

The approach we follow basically amounts to directly solving the equation of motion for the capillary system endowed with thermal fluctuations. In order to interpret the results, a reference nucleation theory is needed. In literature classical nucleation theory (CNT) is the standard choice [10]. In CNT, the two phase system comprising an isolated bubble immersed in the metastable liquid is described by the so-called sharp-interface model where, at fixed temperature, the density field is piecewise continuous, with the density of the liquid outside and that of vapor inside the bubble. CNT determines the size of the critical bubble, corresponding to the transition state. It may happen that the size of the critical bubble is so small to be comparable with the physical thickness of the interface. In such conditions the predictions of CNT can be inaccurate. In order to consider a nucleation theory consistent with our diffuse interface approach, which takes into account the actual thickness of the interface, a more sophisticated theory is needed. Hence, besides CNT, we will use the so-called string method applied to the diffuse interface model to identify the critical state and the transition path leading from the metastable liquid to the cavitated vapor. The two reference nucleation theories will be used to interpret the results of the direct simulation of the nucleation process. In such a comparison, one should keep in mind that the actual process we simulate is typically significantly more complex than assumed in the reference theories. In particular, at least three effects which are neglected in the ordinary approaches are taken into consideration by our simulations: (1) several bubbles are simultaneously present in the system, (2) there is a dynamical interaction between the bubbles, and (3) temperature is a field, which may fluctuate in time and space due to several reasons, namely, the stochastic forcing itself and, more significantly, the intrinsic dynamics of the bubbles, including expansion, compression, and latent heat release, all of which are included in our description.

The paper is structured as follows: in Sec. II we discuss the mathematical aspects of the two-phase modeling. First, in Sec. II A we address the diffuse interface approach exploited to describe vapor-liquid systems embedded with capillarity effects. A purely thermodynamic analysis allows us to obtain important information about the properties of critical nuclei, in particular the critical bubble radius and the energy barrier required for the transition from the metastable liquid to the nucleated vapor bubble. The issue is addressed through the application of the string method [28] illustrated

in Sec. II B. In Sec. II C we introduce fluctuating hydrodynamics in the context of the diffuse interface approach. The model consists in a set of stochastic partial differential equations (SPDEs). The specialist aspects are derived in full detail in Appendixes A and B, respectively devoted to a discussion of the equilibrium statistical properties of the fluctuating field and to the specific form the fluctuation-dissipation balance takes in the present context. Section III deals with the numerical simulations. More specifically, Sec, III A illustrates the properties of the numerical scheme, and Sec. III B addresses bubble nucleation results, with particular attention to nucleation rate, bubble volume distribution and bubble-bubble interaction effects during the process. Finally Sec. IV is devoted to our conclusions and to the open problems in the field.

II. MATHEMATICAL MODEL

A. Diffuse interface approach for vapor-liquid systems

The diffuse interface modeling adopted here has a strict relationship with more fundamental atomistic approaches, since it is based on a suitable approximation of the free energy functional derived in DFT [12]. It dates back to the famous Van der Waals square gradient approximation of the Helmholtz free energy functional

$$F[\rho,\theta] = \int_V f\, dV = \int_V \left[f_b(\rho,\theta) + \frac{1}{2}\lambda \nabla\rho\cdot\nabla\rho \right] dV, \tag{1}$$

where f_b is the classical bulk free energy density, expressed as a function of density ρ and temperature θ. λ is the capillarity coefficient that controls the (equilibrium) surface tension γ and interface thickness. In particular the temperature dependent surface tension can be obtained as [12,29]

$$\gamma(\theta) = \int_{\rho_v^{sat}(\theta)}^{\rho_l^{sat}(\theta)} \sqrt{2\lambda[f_b(\rho,\theta) - f_b(\rho_v^{sat}(\theta),\theta) - \mu_b(\rho,\theta)\rho + \mu^{sat}(\theta)\rho_v^{sat}(\theta)]}\, d\rho, \tag{2}$$

with $\mu_b = \partial f_b/\partial\rho|_\theta$ the bulk chemical potential and the superscript *sat* denoting saturation conditions. In this work we will compare our numerical simulations with results obtained with molecular dynamics of Lennard-Jones (LJ) fluids; hence for a fair comparison we adopted as bulk free energy $f_b(\rho,\theta)$ the modified Benedict-Webb-Rubin equation of state (MBWR EoS) that well reproduces the thermodynamic properties of an LJ fluid [30]. All quantities are made dimensionless according to $\rho^* = \rho/\rho_r$, $\theta^* = \theta/\theta_r$, by introducing as reference quantities the parameters of the LJ potential, $\sigma = 3.4\times10^{-10}$, m as length, $\epsilon = 1.65\times10^{-21}$, J as energy, $m = 6.63\times10^{-26}$, kg as mass, and $\theta_r = \epsilon/k_B$ as temperature. In the left panel of Fig. 1 we compared the temperature dependence of the surface tension obtained through application of Eq. (2) coupled with the MBWR EoS and some benchmark values obtained through Monte Carlo simulations. In order to reproduce the benchmark results we fixed the value of the capillary coefficient to $\lambda^* = \lambda m^2/(\sigma^5\epsilon) = 5.224$. It is worthwhile stressing that a constant coefficient is sufficient to reproduce the correct temperature dependence of the surface tension. Hereafter the asterisk will be omitted to simplify notation.

B. Transition path and the critical bubble

The minimization of the free energy functional (1), stating that the generalized chemical potential $\mu_c = \mu_c^b(\rho) - \lambda\nabla^2\rho$ must be constant and equal to the external chemical potential μ_{ext}, allows the evaluation of the equilibrium density profiles at the different thermodynamic conditions. Clearly, in thermodynamic conditions where either the liquid or the vapor is stable, constant chemical potential corresponds to a homogeneous phase. When the liquid or the vapor is metastable instead three solutions at constant chemical potential are found: (1) the homogeneous vapor, (2) the homogeneous liquid, and (3) a two-phase solution with a spherical (critical) nucleus of a given radius (vapor or liquid in the case of bubble or droplet, respectively), the critical nucleus being surrounded by the metastable phase.

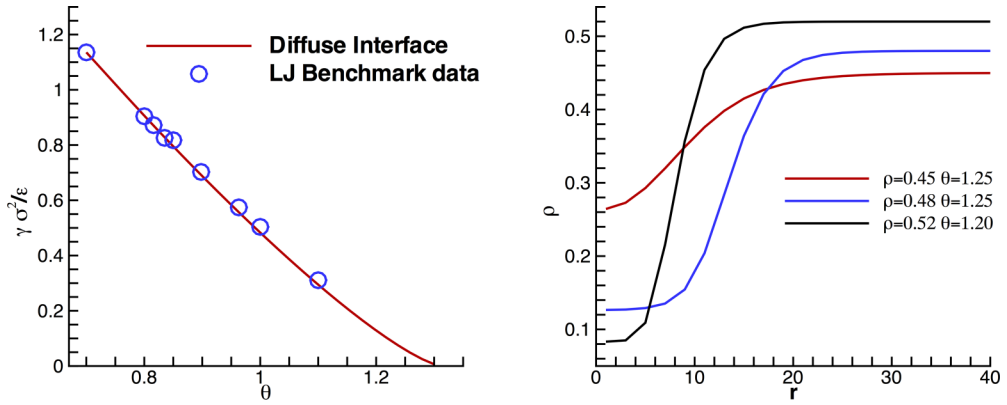

FIG. 1. Left panel: Comparison between the temperature dependence of the surface tension obtained through Eq. (2), when using the Lennard-Jones EoS [30], and the benchmark data provided at Ref. [31]. The value of the capillary coefficient is fixed to $\lambda m^2/(\sigma^5\epsilon) = 5.224$. Right panel: Density profiles of the critical nuclei, evaluated with the string method, at different thermodynamic conditions of the metastable liquid.

Dealing with nucleation, the nontrivial solution of case (3), $\rho(r) = \rho_{\rm crit}(r)$ where the critical bubble is surrounded by the metastable liquid at $\rho = \rho_L^{\rm met}$, $\theta = \bar{\theta}$ and $\mu_c(\rho_L^{\rm met},\bar{\theta}) = \mu^{\rm met}$ is particularly significant. The solution $\rho(r) = \rho_{\rm crit}(r)$ is found by solving the nonlinear Euler-Lagrange equation of the functional 1, which, in spherical coordinates and at fixed temperature, reads

$$\mu_c^b(\rho,\bar{\theta}) - \frac{\lambda}{r^2}\frac{\partial}{\partial r}\left(r^2\frac{\partial \rho}{\partial r}\right) = \mu^{\rm met}. \tag{3}$$

The critical bubble, $\rho_c(r)$, is an unstable solution of Eq. (3), which requires specialized numerical techniques. In this work we applied the powerful string method [28], which, as a by-product, identifies the transition path joining the metastable liquid to the cavitated (stable) vapor. The transition path can be visualized as the continuous sequence of density configurations, $\rho(r,\alpha)$, the system assumes when transitioning from the metastable to the stable state, where α is a suitably defined parameter along the path. The distance between two configurations is expressed as

$$\Delta\ell = \sqrt{\frac{1}{V}\int \Delta\rho^2(r)\,dV} \tag{4}$$

and defines the arclength along the path. The discrete form of the path, consisting of a finite number of configurations, is called the *string*. The string method numerically approximates the transition path starting from an initial set of N_s configurations $\{\rho^k(r)\}$, which form the initial guess for the discretized transition path. The head of the string ($k = 1$) is initialized as a uniform density field corresponding to the uniform metastable liquid $\rho(r) = \rho_L^{\rm met}$; the tail ($k = N_s$) is initialized as a guessed tanh-density profile adjoining the liquid and the vapor density to approximate a vapor bubble. All the intermediate images on the string are obtained by interpolation of these two density fields with respect to the above defined arclength. The algorithm used to relax the string to its final configuration corresponding to the actual transition path follows two steps. (1) All the images $\rho^k(r)$ are evolved over one pseudo-time step $\Delta\tau$ following the steepest-descent algorithm

$$\frac{\partial \rho}{\partial \tau} = \mu^{\rm met} - \left[\mu_c^b(\rho) - \frac{\lambda}{r^2}\frac{\partial}{\partial r}\left(r^2\frac{\partial \rho}{\partial r}\right)\right]. \tag{5}$$

(2) The images are redistributed along the string following a reparametrization procedure by equal arclength. The algorithm is arrested when the string converges within a prescribed error.

TABLE I. Comparison between CNT and the string method applied to the diffuse interface model. Critical radii and (Landau) free energy barriers $\widetilde{\Delta\Omega}$ for bubble nucleation from the liquid. The discrepancy close to the spinodal and at higher temperature are well known from the literature.

θ_0	ρ_L^{met}	R_c	R_c^{CNT}	$\widetilde{\Delta\Omega}/\theta_0$	$\widetilde{\Delta\Omega}^{\mathrm{CNT}}/\theta_0$
1.25	0.45	12.04	8.07	2.99	12.89
1.25	0.46	11.16	8.42	11.21	14.05
1.25	0.47	11.85	9.17	22.81	16.67
1.25	0.48	14.18	10.64	43.5	22.41
1.20	0.51	8.28	6.35	19.20	18.13
1.20	0.52	8.79	6.93	33.58	21.60

The density profile of the critical nucleus, plotted in the right panel of Fig. 1 at different metastable conditions, allows the evaluation of the critical radius, by following the relation [32]:

$$R_c = \frac{\int_0^\infty r(\partial\rho_c/\partial r)^2 r^2\, dr}{\int_0^\infty (\partial\rho_c/\partial r) r^2\, dr}, \tag{6}$$

and the evaluation of the energy barrier

$$\widetilde{\Delta\Omega} = \int_0^\infty \left\{ f[\rho_c(r)] - f\left(\rho_L^{\mathrm{met}}\right) - \mu^{\mathrm{met}}\left[\rho_c(r) - \rho_L^{\mathrm{met}}\right]\right\} 4\pi r^2\, dr, \tag{7}$$

defined as the difference in grand potential Ω between the critical nucleus and the metastable liquid.

The results of the string method are compared in Table I with those obtained by CNT, which yields the estimate $\widetilde{\Delta\Omega}^{\mathrm{CNT}} = 4/3\pi\gamma R_c^2$. The data show that CNT underestimates the energy barrier at high temperature while it overestimates it near the spinodal [33].

C. Fluctuating hydrodynamics: The Landau-Lifshitz–Navier-Stokes model embedded with capillarity

The deterministic time evolution of the two-phase, vapor-liquid system obeys mass, momentum, and energy conservation. The thermodynamic considerations of Sec. II A embed capillary effects in the equilibrium model. Following the procedure of nonequilibrium thermodynamics [34], which can be nowadays considered a standard approach, the description is straightforwardly extended to dynamic conditions. New stress and energy flux contributions arise from the capillary term in the free energy [Eq. (1)]. In particular (see Refs. [29,35] for the detailed derivation) the stress tensor reads

$$\boldsymbol{\Sigma} = \left[-p + \frac{\lambda}{2}|\nabla\rho|^2 + \lambda\rho\nabla\cdot(\lambda\nabla\rho)\right]\boldsymbol{I} - \lambda\nabla\rho\otimes\nabla\rho + \mu\left[(\nabla\mathbf{u} + \nabla\mathbf{u}^T) - \frac{2}{3}\nabla\cdot\mathbf{u}\boldsymbol{I}\right], \tag{8}$$

with $p = -\rho^2\partial(f_b/\rho)/\partial\rho = f_b - \mu_c^b\rho$ the pressure and μ the dynamic viscosity. The energy flux entering the energy equation is augmented with a capillarity term which adds to the standard Fourier contribution,

$$\boldsymbol{q} = \lambda\rho\nabla\rho\nabla\cdot\mathbf{u} - k\nabla\theta, \tag{9}$$

with k the thermal conductivity.

Thermal fluctuations needs to be included in the classical hydrodynamic equations in order to describe fluid motion at mesoscopic scale. Based on phenomenological arguments, the theory of fluctuating hydrodynamics was originally developed by Landau and Lifshitz [18] to be later framed in the general contest of stochastic processes [19]. Landau and Lifshitz's original idea was to treat the

thermodynamic fluxes, namely, stress tensor and energy flux, as stochastic processes. As prescribed by the thermodynamics of irreversible processes at a macroscopic level, thermodynamic fluxes are the expression of microscopic molecular degrees of freedom of the thermodynamic system. Under this respect dissipation in fluids can be seen as the macroscopic manifestation of the energy transfer arising from random molecular interactions. Thus at mesoscopic scale, thermodynamic fluxes have to be modeled as stochastic tensor fields, whose statistical properties can be inferred by enforcing the *fluctuation-dissipation balance* (FDB). The detailed derivation of the stochastic contributions is postponed to Appendices A and B. Here we summarize the main aspects of the model. The stochastic evolution of the system is described by the conservation laws of mass, momentum and energy,

$$\begin{aligned} \frac{\partial \rho}{\partial t} + \boldsymbol{\nabla}\cdot(\rho\mathbf{u}) &= 0, \\ \frac{\partial \rho\mathbf{u}}{\partial t} + \boldsymbol{\nabla}\cdot(\rho\mathbf{u}\otimes\mathbf{u}) &= \boldsymbol{\nabla}\cdot\boldsymbol{\Sigma} + \boldsymbol{\nabla}\cdot\boldsymbol{\delta\Sigma}, \\ \frac{\partial E}{\partial t} + \boldsymbol{\nabla}\cdot(\mathbf{u}E) &= \boldsymbol{\nabla}\cdot(\boldsymbol{\Sigma}\cdot\mathbf{u} - \mathbf{q}) + \boldsymbol{\nabla}\cdot(\boldsymbol{\delta\Sigma}\cdot\mathbf{u} - \boldsymbol{\delta q}), \end{aligned} \tag{10}$$

where $\mathbf{u}$ is the fluid velocity, E is the total energy density, $E = \mathcal{U} + 1/2\rho|\mathbf{u}|^2 + 1/2\lambda|\boldsymbol{\nabla}\rho|^2$, with $\mathcal{U}$ the internal energy density. In the momentum and energy equations, $\boldsymbol{\Sigma}$ and $\mathbf{q}$ are the classical deterministic stress tensor and energy flux, respectively, defined in Eqs. (8) and (9), while the terms with the prefix δ are the stochastic parts, required to satisfy the FDB. Enforcing the fluctuation-dissipation balance, the covariance of the stochastic fluxes follows as

$$\langle \boldsymbol{\delta\Sigma}(\hat{x},\hat{t}) \otimes \boldsymbol{\delta\Sigma}^{\dagger}(\tilde{x},\tilde{t})\rangle = \mathbf{Q}^{\Sigma}\delta(\hat{x}-\tilde{x})\delta(\hat{t}-\tilde{t}), \tag{11}$$

and

$$\langle \boldsymbol{\delta q}(\hat{x},\hat{t}) \otimes \boldsymbol{\delta q}^{\dagger}(\tilde{x},\tilde{t})\rangle = \mathbf{Q}^{\mathbf{q}}\delta(\hat{x}-\tilde{x})\delta(\hat{t}-\tilde{t}), \tag{12}$$

where ${\mathbf{Q}^{\Sigma}}_{\alpha\beta\nu\eta} = 2\mathrm{k}_B\theta\mu(\delta_{\alpha\nu}\delta_{\beta\eta} + \delta_{\alpha\eta}\delta_{\beta\nu} - 2/3\delta_{\alpha\beta}\delta_{\nu\eta})$ and ${\mathbf{Q}^{\mathbf{q}}}_{\alpha\beta} = 2\mathrm{k}_B\theta^2 k\delta_{\alpha\beta}$, with k_B the Boltzmann constant. Thanks to the Curie-Prigogine principle [34], the cross-correlation between different tensor rank fluxes vanishes, i.e., $(\langle \delta\mathbf{q}^{\dagger}(\tilde{x},\tilde{t}) \otimes \delta\Sigma(\hat{x},\hat{t})\rangle = 0)$.

Even in equilibrium conditions, thermal noise forces the different fields to fluctuate. The complete (equilibrium) correlation tensor $\mathbf{C}_{\boldsymbol{\Delta}}(\hat{\mathbf{r}},\tilde{\mathbf{r}}) = \langle \boldsymbol{\Delta}(\hat{\mathbf{r}}) \otimes \boldsymbol{\Delta}^{\dagger}(\tilde{\mathbf{r}})\rangle$, with the field fluctuations organized in a five-component vector $\boldsymbol{\Delta}(\mathbf{r}) = \{\delta\rho(\mathbf{r}),\delta\mathbf{u}(\mathbf{r}),\delta\theta(\mathbf{r})\}$, is found to be (see Appendix A)

$$\mathbf{C}_{\boldsymbol{\Delta}}(\hat{\mathbf{r}},\tilde{\mathbf{r}}) = \begin{pmatrix} C_{\delta\rho\delta\rho} & 0 & 0 \\ 0 & \mathbf{C}_{\delta\mathbf{u}\delta\mathbf{u}} & 0 \\ 0 & 0 & C_{\delta\theta\delta\theta} \end{pmatrix}, \tag{13}$$

with

$$C_{\delta\rho\delta\rho}(\hat{\mathbf{r}},\tilde{\mathbf{r}}) = \frac{\mathrm{k}_B\theta_0}{4\pi\lambda|\hat{\mathbf{r}}-\tilde{\mathbf{r}}|}\exp\left(-|\hat{\mathbf{r}}-\tilde{\mathbf{r}}|\sqrt{\frac{c_T^2}{\rho_0\lambda}}\right), \tag{14}$$

$$\mathbf{C}_{\delta\mathbf{u}\delta\mathbf{u}}(\hat{\mathbf{r}},\tilde{\mathbf{r}}) = \frac{k_B\theta_0}{\rho_0}\mathbf{I}\delta(\hat{\mathbf{r}}-\tilde{\mathbf{r}}), \tag{15}$$

$$C_{\delta\theta\delta\theta}(\hat{\mathbf{r}},\tilde{\mathbf{r}}) = \frac{k_B\theta_0^2}{\rho_0 c_v}\delta(\hat{\mathbf{r}}-\tilde{\mathbf{r}}). \tag{16}$$

In these equations ρ_0 and θ_0 are the equilibrium density and temperature, respectively, $c_T^2 = \partial p/\partial\rho|_T$ the isothermal speed of sound, and c_v the specific heat at constant volume. It is worth noting that the spatial correlation of density fluctuations arise from the long range capillary interactions and is not spatially δ-correlated as usual in simple fluids [36].

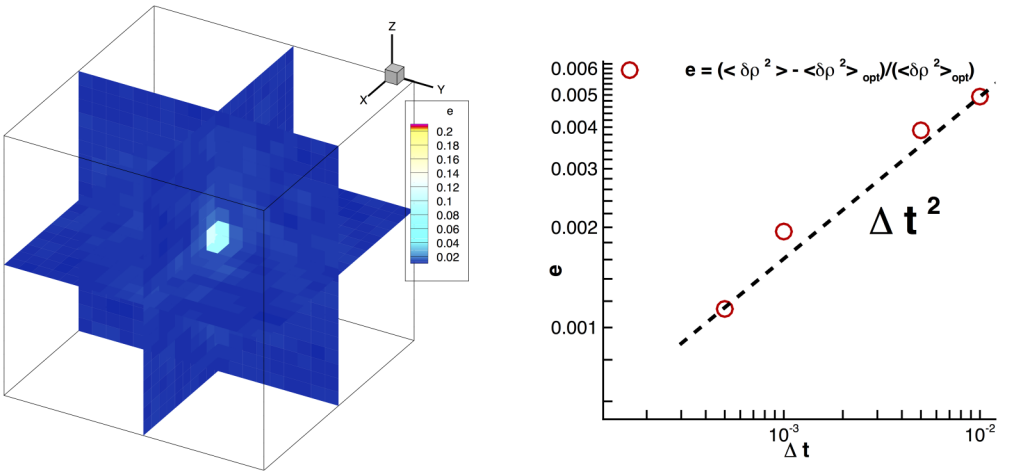

FIG. 2. Left panel: Static structure factor comparison for a capillary fluid in a 3D system. We report the relative error $e = |S_f - S_t|/S_t$ between the theoretical prediction and numerical calculation for each wave numbers k_x,k_y,k_z in the Fourier space. Right panel: Error of the density variance at different simulation time steps. As expected, the error follows a square power law $e \propto \Delta t^2$.

III. RESULTS AND DISCUSSION

A. Stochastic pde's and numerical integration

System (10) has been discretized in the spirit of the method of lines, which consists of two stages: spatial discretization and temporal integration, respectively. Concerning spatial discretization, the different physical phenomena described by the LLNS system ask for specialized numerical techniques. A crucial point is the correct reproduction of the statistical properties at the discrete level [37], consistency with fluctuation-dissipation balance in particular. Equations (10) have been discretized on a uniformly spaced staggered grid, following Ref. [20]. Due to staggering, scalar fields, e.g., density, are located at the cell center, while components of vector fields in a given direction are located at the center of the perpendicular face.

The numerical scheme has been validated by comparing the numerical equilibrium static correlations with the theoretical ones in the discretized equations. Here we report the comparison of the density static structure factor, which is the Fourier transform of the static correlation function $C_{\delta\rho\delta\rho}$ in Eq. (14). In the discrete limit, the theoretical static structure factor reads

$$S_t(\mathbf{k_d}) = \frac{\rho_0 k_B \theta_0}{c_T^2 + \rho_0 \lambda \mathbf{k_d} \cdot \mathbf{k_d}}, \tag{17}$$

where

$$\mathbf{k_d} \cdot \mathbf{k_d} = \left[\frac{\sin(k_x \Delta x/2)}{\Delta x/2}\right]^2 + \left[\frac{\sin(k_y \Delta y/2)}{\Delta y/2}\right]^2 + \left[\frac{\sin(k_z \Delta z/2)}{\Delta z/2}\right]^2 \tag{18}$$

is the discrete version of the square norm of $\mathbf{k}$, arising from the discrete Laplacian operator in Fourier space [26]. The numerical estimate of the density structure factor is calculated, following its definition, as

$$S_f(\mathbf{k_d}) = \langle \delta\rho(\mathbf{k_d}) \delta\rho^*(\mathbf{k_d}) \rangle, \tag{19}$$

where dependency on the wave number implicitly denotes Fourier components.

As shown in the left panel of Fig. 2, numerical results are in very good agreement with the theoretical prediction. In particular the relative error e is almost everywhere less than 2%–3% in the

TABLE II. Numerical temperature and velocity variances in comparison with theoretical values.

Variances	Theoretical prediction	Numerical value	Error %
$\langle \delta u_x^2 \rangle$	1.3333×10^{-4}	1.3332×10^{-4}	0.01
$\langle \delta u_y^2 \rangle$	1.3333×10^{-4}	1.3331×10^{-4}	0.02
$\langle \delta u_z^2 \rangle$	1.3333×10^{-4}	1.3335×10^{-4}	0.02
$\langle \delta \theta^2 \rangle$	5.8361×10^{-5}	5.8443×10^{-5}	0.15

field, except for the small wave numbers, due to the slow convergence of low wavelength modes [26]. Nevertheless, even in the latter case, the relative error is less then 10%. As a second test, we compared the variance of velocity and temperature fluctuations. In particular, the velocity fluctuations must reproduce the celebrated equipartition theorem, here reported in the discrete version:

$$\langle \delta \mathbf{u} \cdot \delta \mathbf{u} \rangle = 3 \frac{k_B \theta_0}{\rho_0 \Delta V}, \tag{20}$$

$$\langle \delta \theta^2 \rangle = \frac{k_B \theta_0^2}{\rho_0 c_v \Delta V}. \tag{21}$$

The values reported in Table II clearly show a perfect matching between numerical results and theoretical expectation.

As a last test, we validated the accuracy of our time integration method. We performed the time evolution by means of a second-order Runge-Kutta scheme [21]. We compared the numerical error, e, on the variance of density fluctuations $\langle \delta\rho(\mathbf{x})^2 \rangle$ at different time steps Δt with respect to $\langle \delta\rho(\mathbf{x})^2 \rangle_{\text{opt}}$ obtained with our finest integration step $\Delta t = 10^{-4}$:

$$e = \frac{|\langle \delta\rho(\mathbf{x})^2 \rangle - \langle \delta\rho(\mathbf{x})^2 \rangle_{\text{opt}}|}{\langle \delta\rho(\mathbf{x})^2 \rangle_{\text{opt}}}, \tag{22}$$

where the average is evaluated as $1/(TV) \int_0^T \int_V \delta\rho(\mathbf{x})^2 \, dV \, dt$ with the time window T fixed as $T = 100$ LJ units. The right panel of Fig. 2 clearly shows the expected power law, $e \propto \Delta t^2$.

All these tests ensure that the numerical scheme correctly reproduces the statistical properties of the system, i.e., the fluctuation-dissipation balance is preserved in the discretized equations.

B. The dynamics of vapor bubble nucleation

Bubble nucleation is investigated in a metastable liquid enclosed in a cubic box with periodic boundary conditions, with fixed volume, total mass, and energy (NVE). The equation of state (EoS) we use, which can be chosen freely among available models, e.g., van der Waals or IAPWS [38] EoS for water, corresponds to a LJ fluid [30] to allow direct comparison with MD simulations. The system volume $V = 600^3$ has been discretized on a uniform grid with 50 cells per direction. After a convergence analysis we found that the chosen grid size, $\Delta x = 12$, is sufficient for a reliable simulation in these thermodynamic conditions. Moreover, because of the extension of the simulated domain 10 runs for each condition, with different values of the seed employed to generate random numbers, provide a well converged statistics.

Among the different conditions we have investigated, we mainly focus here on the initial temperature $\theta_0 = 1.25$ at changing bulk density to explore the corresponding metastable range $\rho_L \in [\rho_{\text{spin}}, \rho_{sat}] = [0.44, 0.51]$, where ρ_{sat} and ρ_{spin} are the saturation and spinodal densities, respectively. A few snapshots of the evolution for two different initial conditions are shown in the left panels of Figs. 3 and 4. Starting from a homogeneous metastable liquid phase, the fluctuations lead the system to spontaneously nucleate vapor bubbles. The nucleii start out with a complex, far from spherical, shape; see, e.g., Ref. [13]. Roughly, when they happen to reach a size larger than

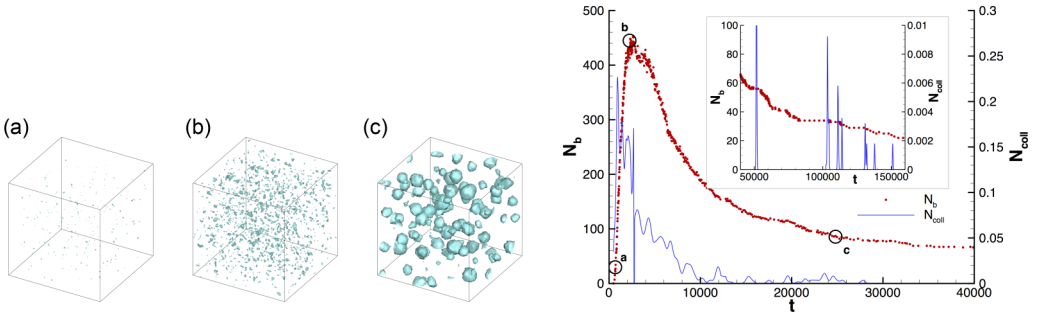

FIG. 3. Left panel: Bubble configurations along nucleation ($\rho = 0.46$, $\theta_0 = 1.25$), from left to right $t = 400$, $t = 2000$, $t = 25\,000$. Animation is available in the Supplemental Material [39]. Right panel: Bubble number evolution (red symbols) and number of coalescence events (blue line).

critical they typically expand. Eventually, after a long and complex dynamics where bubbles expand and coalesce, stable equilibrium conditions are reached. The existence of such equilibrium is due to the constraint on volume and mass of the system. Note that, most often, nucleation is addressed in the grand-canonical ensemble, where volume and chemical potential are specified. The eventual configuration is characterized by several vapor bubbles in equilibrium with the surrounding liquid. The case at $\rho_L = 0.46$, the closest one to the spinodal we considered here, is the most populated, as seen in Fig. 3 compared with Fig. 4. This system has a barrier lower than those further from the spinodal (see Table I), hence it nucleates faster. The initial (metastable) thermodynamic condition also influences the number and typical dimension of the bubbles in the final stage, the right panels of Figs. 3 and 4 providing the bubble number N_b as a function of time.

A tracking procedure has been put forward to follow the evolution of the distinct bubbles. By monitoring bubble volume, mass, center of mass, and its velocity, the tracking algorithm allows for detecting coalescence events. The actual number of collisions between bubbles $\tilde{N}_{\rm coll}$ evaluated at each time step is characterized by a highly discontinuous fingerprint. We smoothed the curve with a Gaussian kernel with standard deviation of order 50 time units to extract more robust indications. The time evolution of the bubble number N_b, Figs. 3 and 4, presents three main phases: (1) the initial *nucleating* phase—when N_b grows linearly with time (i.e., at a constant nucleation rate); (2) the *collapsing* phase during the first part of the expansion stage—characterized by a rapidly decreasing number of bubbles mainly due to collapse; and (3) a *slowly expanding* phase characterizing the long-time dynamics of the multibubble system. The smoothed number of collisions $N_{\rm coll}$, plotted with the blue line in the figures, shows a strong correlation with the number of bubbles throughout the nucleating phase and the collapsing phase. Nucleating and collapsing phases are characterized by

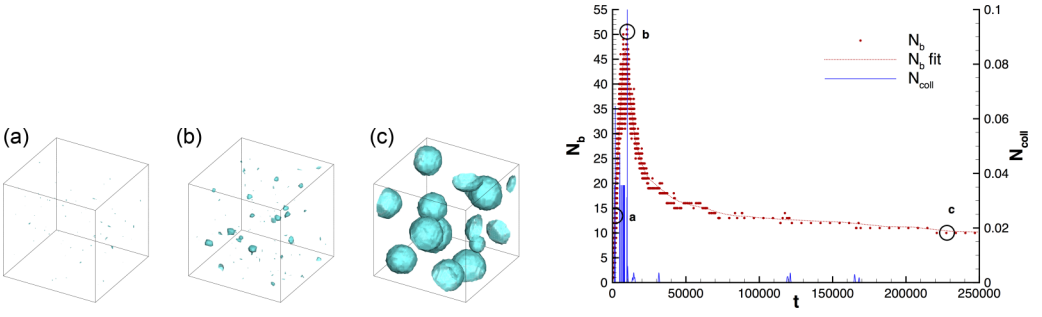

FIG. 4. Same as Fig. 3 at $\rho = 0.48$, $\theta_0 = 1.25$. Snapshots taken at $t = 2000$, $t = 11\,000$, $t = 230\,000$. The bubble number vs time in the right panel is fitted by the dotted red line for better readability.

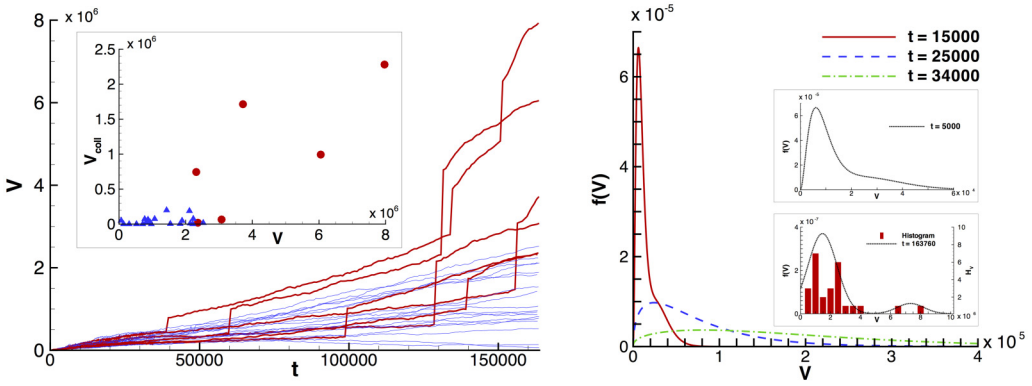

FIG. 5. Left panel: Volume history of the bubbles surviving the entire simulation ($\rho = 0.46$ and $\theta_0 = 1.25$). Intense coalescence events, characterized by a sudden volume jump, are identified in the red curves. The corresponding volumes are shown by the red dots in the inset providing the $V - V_{\text{coll}}$ scatter plot, where V_{coll} is the volume acquired by coalescence. The largest bubbles experienced intense coalescence events. Right panel: Probability distribution function $f(V)$ of the bubble volumes during the nucleation, at different times ($\theta_0 = 1.25$, $\rho = 0.46$, critical volume $V_c = 4445$).

a competing-growth mechanism [40] due to the constraints of constant mass and volume, explaining the high number of supercritical bubble collapses. The coalescence events start being less and less probable during the slowly expanding phase. The inset of the Fig. 3 zooms into this phase showing that isolated collision events still occur, contributing to important acceleration toward the final equilibrium condition.

The volume history of the distinct bubbles (in particular those survived up to the last time investigated) have been plotted in the left panel of Fig. 5. Among the different bubble evolutions, we highlight in red the volume histories of those bubbles that experienced intense coalescence events, characterized by a sudden increase in volume. It is apparent that the larger bubbles gained a substantial part of their volume by coalescence. To substantiate this impression, for each bubble in the last configuration, the sum of the volumes acquired by coalescence throughout the whole evolution, V_{coll}, was calculated in the inset of left Fig. 5. The present mesoscale approach allows us to access the statistics of bubble dimensions. The probability distribution function of bubble volumes $f(V)$ is plotted in the right panel of Fig. 5. During both the *nucleating* and *collapsing* phases the pdf is sharply peaked at small volumes, of the order of 2–4 V_c. The successive bubble expansion phase is substantially slower and calls for a much longer observation time to detect a significant growth (green dash-dotted curve at $t = 34\,000$). The intense coalescence events explain the presence of the second peak in the pdf at very large volume (black curve in the inset on the right panel of Fig. 5 at $t = 163\,760$).

The initial *nucleating* stage, where the bubble number increases linearly, gives access to the nucleation rate J in terms of bubbles formed per unit time and volume. It is here calculated as the slope of the linear fit to the curves of Figs. 3 and 4 near the origin. The results are plotted in Fig. 6, which also provides a direct comparison with some MD simulations [13,41]. The values agree comfortably well with molecular dynamic simulations in the NVE ensemble. As is common in literature, the present results are compared also with CNT prediction for the nucleation rate, $J_{\text{CNT}} = n_L\sqrt{2\gamma/m\pi}\exp(-\widetilde{\Delta\Omega}^{\text{CNT}}/k_B\theta)$, where n_L is the liquid number density. The expression of the energy barrier was already explicitly given in Sec. II B while the preexponential factor is taken in the classical form proposed by Blander and Katz [10] and already used in Ref. [13] as a reference for a large number of MD simulations. It is worth noting that the energy barriers estimated from CNT and from the string method (Table I) are strongly based on the assumption that only a single bubble can nucleate. As already discussed when commenting on the coalescence events, in

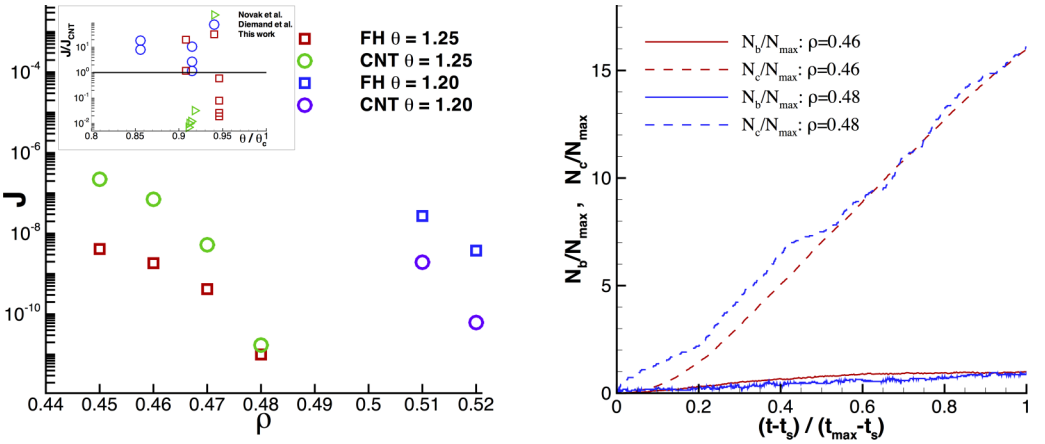

FIG. 6. Left panel: Comparison of the nucleation rate obtained via FH simulations (red squares at $\theta_0 = 1.25$ and blue squares at $\theta_0 = 1.20$) with respect to CNT predictions (green circles at $\theta_0 = 1.25$ and purple circles at $\theta_0 = 1.20$). The inset shows the comparison with other authors. Right panel: Time evolution of the number of supercritical bubbles N_b and the total collapsed supercritical bubble N_c up to time instant t. The number of bubbles is rescaled with the maximum number of bubble observed during the simulation, $N_{\max}$, which correspond to $N_{\max} = 458$ in the thermodynamic condition with $\rho_L = 0.46$ and $N_{\max} = 52$ in the case with $\rho_L = 0.48$. The time is shifted and rescaled in such a way that all the curves start when the first bubble appears, at $t = t_s$, and finish when $N_{\max}$ is reached, at $t = t_{\max}$.

the thermodynamic conditions we studied the effects of bubble-bubble interaction are instead crucial to understand the full dynamics of the bubble evolution. In particular, the conditions assumed in our present simulations and in the MD simulations used for comparison correspond instead to given system volume, energy, and mass—the NVE ensemble—and the system is free to simultaneously nucleate several bubbles. The consequence of fixing the mass of the system is that the larger is the overall volume of the different bubbles that are simultaneously nucleated the more the liquid is compressed. As a result the nucleation process is discouraged. To further substantiate the importance of this point we evaluated the number of collapsed bubble after crossing the critical size. The total number, up to the current time, is plotted in the right panel of Fig. 6 labeled as N_c. If no collapse occurred, the total number of bubbles in the system would have been $N_{\text{tot}} = N_b + N_c$ and the rate would have been larger by roughly a factor 15.

IV. CONCLUSIONS

In conclusion, the FH approach together with a diffuse interface modeling of the multiphase system have been exploited to study homogeneous nucleation of vapor bubbles in metastable liquids. We evaluated the nucleation rate and compared it favorably with state-of-the-art simulations. Concerning the comparison with classical approaches, CNT, and the string method for the diffused interface model, we found that the simultaneous nucleation of several bubbles has a strong effect on the nucleation rate, which is found to be altered with respect to the above single-bubble models. The present technique has revealed extremely cheaper with respect to MD simulations, allowing the analysis of the very long bubble expansion stage where bubble-bubble interaction and coalescence events turn out to determine the eventual bubble size distribution. The accurate results and the efficiency of the modeling encourage the exploitation for more complex conditions, e.g., heterogeneous nucleation and multispecies systems, and could pave the way for the development of innovative continuum formulation to address thermally activated processes.

ACKNOWLEDGMENTS

The research leading to these results has received funding from the European Research Council under the European Union's Seventh Framework Programme (FP7/2007-2013)/ERC Grant no. 339446.

APPENDIX A: STATIC CORRELATION FUNCTIONS

The static correlation functions of a thermodynamic system in equilibrium can be evaluated from the entropy deviation ΔS from its equilibrium value S_0. For single-component systems ΔS can be expressed as a functional of fluctuating fields of mass density, $\delta\rho(\mathbf{x},t)$, velocity, $\delta\mathbf{u}(\mathbf{x},t)$, and temperature, $\delta\theta(\mathbf{x},t)$,

$$\Delta S = S - S_0 = \Delta S[\delta\rho,\delta\mathbf{u},\delta\theta] = \int_V [s(\mathbf{x},t) - s_0]\, dV, \tag{A1}$$

where the integration is over the system volume V, $s(\mathbf{x},t)$ is the entropy density per unit volume, and s_0 is its equilibrium value (i.e., S_0 is the entropy maximum). The actual entropy maximum must respect the constraint of given total mass (M_0) and given total energy (E_0), if we are interested in the study of closed and isolated systems. Hence the correct functional to be maximized at equilibrium is the constrained entropy ΔS_c expressed as

$$\Delta S_c = \Delta S + k_1\left(M_0 - \int_V \rho\, dV\right) + k_2\left(E_0 - \int_V e\, dV\right), \tag{A2}$$

where k_1 and k_2 are the two Lagrange multipliers. In order to describe the two-phase liquid-vapor system we adopted the Van der Waals square gradient approximation of the free energy functional, Eq. (1), that we here repeat for the reader's convenience:

$$F[\rho,\theta] = \int_V dV\left[f_b(\rho,\theta) + \frac{1}{2}\lambda\nabla\rho\cdot\nabla\rho\right], \tag{A3}$$

where f_b is the classical bulk free energy density and λ is the capillary coefficient, controlling both the surface tension and the interface thickness. The entropy functional S is related to the functional derivative of the free energy with respect to temperature

$$S[\rho,\theta] = \int_V -\frac{\delta F}{\delta\theta}\, dV = \int_V -\frac{\partial f_b}{\partial\theta}\, dV = \int_V s_b(\rho,\theta)\, dV, \tag{A4}$$

where the second equality holds if λ does not depend on temperature, and the last identity follows by the classical definition of the bulk entropy density s_b. Thus the constrained functional expressed in Eq. (A2), reads

$$\Delta S_c = \Delta S_b + k_1\left(M_0 - \int_V \rho\, dV\right) + k_2\left(E_0 - U - \int_V \frac{1}{2}\rho\mathbf{u}\cdot\mathbf{u}\, dV\right), \tag{A5}$$

where the internal energy functional U is defined in terms of free energy as

$$U = F - \int dV \frac{\delta F}{\delta\theta}\theta = \int_V dV\left[u_b(\rho,\theta) + \frac{1}{2}\lambda\nabla\rho\cdot\nabla\rho\right], \tag{A6}$$

with $u_b = f_b - \theta\partial f_b/\partial\theta$ the bulk internal energy density. The two Lagrange multipliers k_1 and k_2 are calculated by imposing that the first variation of the functional in Eq. (A5) evaluated in the equilibrium state must be zero:

$$\delta\Delta S_c[\rho_0,\mathbf{0},\theta_0] = 0. \tag{A7}$$

The above equation leads to $k_1 = -\mu_{c,0}/\theta_0$, $k_2 = 1/\theta_0$, where $\mu_{c,0}$ is the equilibrium chemical potential, and $\mu_c^b = \partial f_b/\partial\rho$ is the *bulk* chemical potential. For small fluctuations, the entropy

functional can be expanded in a Taylor series around the equilibrium value, with respect to the variables $\mathbf{U} = (\rho, \nabla\rho, \ldots, \nabla^n\rho, \theta, \mathbf{u})^T$, as follows:

$$\begin{aligned}\Delta S_c &= \int_V \Delta s_c(\rho, \nabla\rho, \ldots, \nabla^n\rho, \theta, \mathbf{u})\, dV \\ &= \int_V dV \left[\sum_i \frac{\partial \Delta s_c}{\partial U_i}\bigg|_0 \delta U_i + \frac{1}{2}\sum_{i,j} \frac{\partial^2 \Delta s_c}{\partial U_i \partial U_j}\bigg|_0 \delta U_i \delta U_j + \cdots \right]. \end{aligned} \tag{A8}$$

All terms appearing in the right hand side of Eq. (A8) can be expressed in terms of suitable thermodynamic coefficients and of the fluctuations of density, temperature, and velocity, e.g.,

$$\begin{aligned} ds_b &= \frac{1}{\theta} du_b - \frac{\mu_b}{\theta} d\rho, \quad du_b = \rho c_v d\theta + \left(\mu_b + \theta \frac{\partial s_b}{\partial \rho}\bigg|_\theta\right) d\rho, \\ d\mu_b &= \frac{c_T^2}{\rho} d\rho + \left(\frac{1}{\rho}\frac{\partial p}{\partial \theta}\bigg|_\rho - \frac{s_b}{\rho}\right) d\theta, \end{aligned} \tag{A9}$$

where c_v is the specific heat at constant specific volume, c_T the isothermal speed of sound, p the pressure.

Assuming that the fluid is very close to equilibrium and the fluctuations are small with respect to the mean value, the entropy functional can be approximated by a quadratic form in the fluctuating fields:

$$\Delta S_c \simeq -\frac{1}{2}\int_V dV \left[\frac{c_{T0}^2}{\theta_0 \rho_0}\delta\rho^2 - \frac{\lambda}{\theta_0}\delta\rho(\nabla^2\delta\rho) + \frac{\rho_0}{\theta_0}\delta\mathbf{u}\cdot\delta\mathbf{u} + \frac{\rho_0 c_{v0}}{\theta_0^2}\delta\theta^2 \right]. \tag{A10}$$

For future reference, it is worth expressing the above integral as

$$\begin{aligned}\Delta S_c \simeq -\frac{1}{2}\int_V \int_V dV_{\mathbf{x}} dV_{\tilde{\mathbf{x}}} \Bigg\{ & \delta\mathbf{v}(\mathbf{x}) \frac{\rho_0}{\theta_0}\delta(\mathbf{x}-\tilde{\mathbf{x}})\cdot\delta\mathbf{v}(\tilde{\mathbf{x}}) \\ & + \delta\rho(\mathbf{x})\left[\frac{c_{T0}^2}{\theta_0\rho_0}\delta(\mathbf{x}-\tilde{\mathbf{x}}) - \frac{\lambda}{\theta_0}\nabla_{\mathbf{x}}^2\delta(\mathbf{x}-\tilde{\mathbf{x}})\right]\delta\rho(\tilde{\mathbf{x}}) + \delta\theta(\mathbf{x})\frac{\rho_0 c_{v0}}{\theta_0^2}\delta(\mathbf{x}-\tilde{\mathbf{x}})\delta\theta(\tilde{\mathbf{x}})\Bigg\}, \end{aligned} \tag{A11}$$

where integration by parts is used twice to move the Laplacian ∇^2 from the density to the Dirac delta function. Eq. (A11) can be rewritten in the operator form

$$\Delta S_c = -\frac{1}{2}\int_V \boldsymbol{\Delta}^\dagger \mathcal{H}\, \boldsymbol{\Delta}\, dV, \tag{A12}$$

where $\boldsymbol{\Delta} = (\delta\rho, \delta\mathbf{u}, \delta\theta)$ is the vector of the the fluctuating fields and $\mathcal{H}$ is a diagonal, positive definite matrix operator

$$\Gamma(\mathbf{x}) = (\mathcal{H}\boldsymbol{\Delta})(\mathbf{x}) = \int_V \mathbf{H}(\mathbf{x},\tilde{\mathbf{x}})\boldsymbol{\Delta}(\tilde{\mathbf{x}})\, dV_{\tilde{\mathbf{x}}} = \int_V \hat{\mathbf{H}}(\mathbf{x})\delta(\mathbf{x}-\tilde{\mathbf{x}})\boldsymbol{\Delta}(\tilde{\mathbf{x}})\, dV_{\tilde{\mathbf{x}}}, \tag{A13}$$

where

$$\hat{\mathbf{H}}(\mathbf{x}) = \begin{pmatrix} \hat{H}_{\delta\rho\delta\rho} & 0 & 0 \\ 0 & \mathbf{I}\hat{H}_{\delta\mathbf{u}\delta\mathbf{u}} & 0 \\ 0 & 0 & \hat{H}_{\delta\theta\delta\theta} \end{pmatrix} = \begin{pmatrix} \frac{c_{T0}^2}{\theta_0\rho_0} - \frac{\lambda}{\theta_0}\nabla_{\mathbf{x}}^2 & 0 & 0 \\ 0 & \frac{\rho_0}{\theta_0}\mathbf{I} & 0 \\ 0 & 0 & \frac{\rho_0 c_{v0}}{\theta_0^2} \end{pmatrix} \tag{A14}$$

involves differential operators and $\mathbf{I}$, the 3×3 identity matrix. Note that, indeed, the Laplace operator $-\nabla^2$ appearing in the first line, which is in general non-negative, is strictly positive under the constraint of mass conservation since the mean spatial density fluctuation is identically zero.

Under these assumptions the more general probability distribution functional for the fluctuating fields $\mathbf{\Delta}$,

$$P_{\rm eq}[\mathbf{\Delta}] = \frac{1}{Z}\exp\left(\frac{\Delta S_c}{k_B}\right), \tag{A15}$$

can be rewritten by using the second order approximation, Eq. (A12),

$$P_{\rm eq}[\mathbf{\Delta}] = \frac{1}{Z}\exp\left(-\frac{1}{2k_B}\int_V \Delta^\dagger \mathcal{H}\,\Delta\, dV\right), \tag{A16}$$

which can be factorized since $\hat{\mathbf{H}}$ is diagonal,

$$P_{\rm eq}[\mathbf{\Delta}] = P_{\delta\rho}[\delta\rho]P_{\delta\mathbf{u}}[\delta\mathbf{u}]P_{\delta\theta}[\delta\theta], \tag{A17}$$

with

$$P_{\delta\rho} = \frac{1}{Z_{\delta\rho}}\exp\left[-\frac{1}{2\mathrm{k}_B}\int\int d\mathbf{x}\,d\mathbf{x}'\delta\rho(\mathbf{x})H_{\delta\rho\delta\rho}\delta(\mathbf{x}-\mathbf{x}')\delta\rho(\mathbf{x}')\right], \tag{A18}$$

$$P_{\delta\mathbf{u}} = \frac{1}{Z_{\delta\mathbf{u}}}\exp\left[-\frac{1}{2\mathrm{k}_B}\int\int d\mathbf{x}\,d\mathbf{x}'\delta\mathbf{u}^T(\mathbf{x})H_{\delta\mathbf{u}\delta\mathbf{u}}\delta(\mathbf{x}-\mathbf{x}')\delta\mathbf{u}(\mathbf{x}')\right], \tag{A19}$$

$$P_{\delta\theta} = \frac{1}{Z_{\delta\theta}}\exp\left[-\frac{1}{2\mathrm{k}_B}\int\int d\mathbf{x}\,d\mathbf{x}'\delta\theta(\mathbf{x})H_{\delta\theta\delta\theta}\delta(\mathbf{x}-\mathbf{x}')\delta\theta(\mathbf{x}')\right], \tag{A20}$$

and is normalized by the constant Z:

$$Z = \int D\delta\rho D\delta\mathbf{u}D\delta\theta\exp\left(-\frac{1}{2k_B}\int_V \mathbf{\Delta}^\dagger\mathcal{H}\mathbf{\Delta}\,dV\right) = Z_{\delta\rho}Z_{\delta\mathbf{u}}Z_{\delta\theta}. \tag{A21}$$

The generic correlation function

$$\mathbf{C}_{\mathbf{\Delta}}(\mathbf{x}) = \langle\mathbf{\Delta}\otimes\mathbf{\Delta}^\dagger\rangle = \frac{1}{Z}\int D\delta\rho D\delta\mathbf{u}D\delta\theta\,\mathbf{\Delta}\otimes\mathbf{\Delta}^\dagger\exp\left[\frac{1}{k_B}\int_V \Delta s(\delta\rho,\delta\mathbf{u},\delta\theta)\,dV\right] \tag{A22}$$

can now be evaluated in closed form by integrating Gaussian path integrals. To this end it is helpful to resort to the characteristic functional [42] of the pdf, which, for a generic process $X(\mathbf{x})$, is

$$\Phi[\chi] = \int DX\ P[X]\exp\left[\int \chi(\mathbf{x})X(\mathbf{x})dV_{\mathbf{x}}\right]. \tag{A23}$$

For a Gaussian process governed by the pdf

$$P[X] = \frac{1}{Z}\exp\left[\int -\frac{1}{2}X(\mathbf{x})A(\mathbf{x},\tilde{\mathbf{x}})X(\tilde{\mathbf{x}})dV_{\mathbf{x}}\,dV_{\tilde{\mathbf{x}}}\right]$$

the characteristic functional reduces to

$$\Phi[\chi] = \int DX\exp\left[-\frac{1}{2}\int\int d\hat{\mathbf{x}}\,d\tilde{\mathbf{x}}X(\hat{\mathbf{x}})A(\hat{\mathbf{x}},\tilde{\mathbf{x}})X(\tilde{\mathbf{x}}) + \int\chi(\hat{\mathbf{x}})X(\hat{\mathbf{x}})d\hat{\mathbf{x}}\right] \tag{A24}$$

and is easily evaluated by completing the square as

$$\Phi[\chi] = \Phi[0]\exp\left[\frac{1}{2}\int\int d\hat{\mathbf{x}}\,d\tilde{\mathbf{x}}\chi(\hat{\mathbf{x}})G(\hat{\mathbf{x}},\tilde{\mathbf{x}})\chi(\tilde{\mathbf{x}})\right], \tag{A25}$$

where

$$G(\hat{\mathbf{x}},\tilde{\mathbf{x}}) = A^{-1}(\hat{\mathbf{x}},\tilde{\mathbf{x}}). \tag{A26}$$

We stress that A is the kernel of an operator $\mathcal{A}$, e.g.,

$$\Gamma = \mathcal{A}\Delta \iff \Gamma(\mathbf{x}) = \int_V A(\mathbf{x},\tilde{\mathbf{x}})\Delta(\mathbf{x})\, dV_{\mathbf{x}},$$

such that A^{-1} should be understood as the kernel of the inverse $\mathcal{A}^{-1}$. As is well known, the two-point correlation can be written in terms of the characteristic functional as

$$C_{XX}(\hat{\mathbf{x}},\tilde{\mathbf{x}}) = \langle X(\hat{\mathbf{x}})X(\tilde{\mathbf{x}})\rangle = \left[\frac{1}{\Phi[0]}\frac{\delta}{\delta\chi(\hat{\mathbf{x}})}\frac{\delta}{\delta\chi(\tilde{\mathbf{x}})}\Phi[\chi]\right]_{\chi=0} = G(\hat{\mathbf{x}},\tilde{\mathbf{x}}). \tag{A27}$$

In the present case, Eq. (A16), the kernel of the operator A is given by

$$A(\hat{\mathbf{x}},\tilde{\mathbf{x}}) = \frac{1}{\mathrm{k}_B}\hat{\mathbf{H}}\delta(\hat{\mathbf{x}}-\tilde{\mathbf{x}}), \tag{A28}$$

implying the equation

$$\int \mathbf{A}(\mathbf{x},\mathbf{x}'')\mathbf{G}(\mathbf{x}'',\mathbf{x}')dV_{\mathbf{x}''} = \frac{1}{\mathrm{k}_B}\int \hat{\mathbf{H}}\delta(\mathbf{x}-\mathbf{x}'')\mathbf{G}(\mathbf{x}'',\mathbf{x}')dV_{\mathbf{x}''} = \hat{\mathbf{U}}\delta(\mathbf{x}-\mathbf{x}'), \tag{A29}$$

which, written in terms of operators, corresponds to the equation $\mathcal{A}\mathcal{A}^{-1} = \mathcal{U}$, with $\mathcal{U}$ the identity operator on the space of fluctuations, and $\hat{\mathbf{U}}$ is the identity matrix acting on the five-dimensional tangent space at a given position $\mathbf{x}$, $\mathbf{\Delta}(\mathbf{x}) = (\delta\rho(\mathbf{x}),\delta\mathbf{u}(\mathbf{x}),\delta\theta(\mathbf{x}))$.

In particular, since the matrix $\hat{\mathbf{H}}$ is diagonal, the $\delta\rho,\delta\rho$ component of the above equation is

$$\int A_{\delta\rho\delta\rho}(\mathbf{x},\mathbf{x}'')G_{\delta\rho\delta\rho}(\mathbf{x}'',\mathbf{x}')dV_{\mathbf{x}''} = \frac{1}{\mathrm{k}_B}\int\left[\left(\frac{c_T^2}{\theta_0\rho_0} - \frac{\lambda}{\theta_0}\nabla^2_{\mathbf{x}}\right)\delta(\mathbf{x}-\mathbf{x}'')\right]$$
$$G_{\delta\rho\delta\rho}(\mathbf{x}'',\mathbf{x}')dV_{\mathbf{x}''} = \delta(\mathbf{x}-\mathbf{x}'). \tag{A30}$$

After integration by parts, Eq. (A30) reads

$$\frac{c_T^2}{\theta_0\rho_0\mathrm{k}_B}G_{\delta\rho\delta\rho}(\hat{\mathbf{x}},\tilde{\mathbf{x}}) - \frac{\lambda}{\theta_0\mathrm{k}_B}\nabla^2_{\hat{\mathbf{x}}}G_{\delta\rho\delta\rho}(\hat{\mathbf{x}},\tilde{\mathbf{x}}) = \delta(\hat{\mathbf{x}}-\tilde{\mathbf{x}}). \tag{A31}$$

The solution (the Green's function for the Helmholtz equation), is formally written as

$$G_{\delta\rho\delta\rho}(\hat{\mathbf{x}},\tilde{\mathbf{x}}) = \int d\mathbf{k}\frac{\mathrm{k}_B\rho_0\theta_0}{c_T^2 + \rho_0\lambda\mathbf{x}\cdot\mathbf{k}}e^{i\mathbf{k}\cdot(\hat{\mathbf{x}}-\tilde{\mathbf{x}})}, \tag{A32}$$

whose inverse Fourier transform yields

$$G_{\delta\rho\delta\rho}(\hat{\mathbf{x}},\tilde{\mathbf{x}}) = C_{\delta\rho\delta\rho}(\hat{\mathbf{x}},\tilde{\mathbf{x}}) \tag{A33}$$
$$= \langle\delta\rho(\hat{\mathbf{x}})\delta\rho(\tilde{\mathbf{x}})\rangle = \frac{\mathrm{k}_B\theta_0}{4\pi\lambda|\hat{\mathbf{x}}-\tilde{\mathbf{x}}|}\exp\left(-|\hat{\mathbf{x}}-\tilde{\mathbf{x}}|\sqrt{\frac{c_T^2}{\rho_0\lambda}}\right),$$

where we have recognized that $\mathbf{G} = \mathbf{C}_{\mathbf{\Delta}}$ [Eq. (A27)]. The same procedure can be used to reconstruct the entire correlation tensor $\mathbf{C}_{\mathbf{\Delta}} = \langle\mathbf{\Delta}\otimes\mathbf{\Delta}^{\dagger}\rangle$ [Eqs. (13)–(16)].

APPENDIX B: FLUCTUATION-DISSIPATION BALANCE

To correctly modeling the stochastic tensor $\boldsymbol{\delta\Sigma}$ and heat flux $\boldsymbol{\delta q}$ we need to recall the fluctuation-dissipation balance (FDB). The system of conservation laws [Eqs. (10)] can be formally rewritten with a more compact notation as

$$\frac{\partial\mathbf{U}}{\partial t} = \mathbf{N}[\mathbf{U}] + \mathbf{f}, \tag{B1}$$

where the components of the generic vector $\mathbf{U}$ are the conserved fields $\mathbf{U} = \{\rho, \rho\mathbf{u}, E\}$, $\mathbf{N}$ is the deterministic nonlinear operator, and $\mathbf{f}$ the stochastic forcing to be determined. In particular $\mathbf{f}(x,t)$ is a Gaussian vector process whose correlation is

$$\langle \mathbf{f}(\tilde{x},t) \otimes \mathbf{f}^{\dagger}(\hat{x},t') \rangle = \mathbf{Q}(\tilde{x},\hat{x})\delta(t-t'), \tag{B2}$$

with $\mathbf{Q}(\tilde{x},\hat{x})$ a matrix depending on $\tilde{x}$ and $\hat{x}$. Note that delta correlation in time is explicitly assumed. The stochastic forcing $\mathbf{f}$ is related to a standard Wiener process $\mathbf{W}dt = d\mathbf{B}$ by the linear relationship

$$\mathbf{f} = \mathbf{K}\mathbf{W}, \tag{B3}$$

where $\mathbf{W} = \{W_\rho, \mathbf{W_u}, W_\theta\}^T$, with $\mathbf{W_u} = (W_{u_x}, W_{u_y}, W_{u_z})^T$ is a Gaussian delta correlated process characterized by the correlation

$$\langle \mathbf{W}(\tilde{y},t) \otimes \mathbf{W}(\hat{y},t') \rangle = \mathbf{I}\delta(\tilde{y}-\hat{y})\delta(t-t'), \tag{B4}$$

with $\mathbf{I}$ a (5×5) identity matrix in the space of $\mathbf{W}$. Finally the linear operator $\mathbf{K}$ takes the form

$$\mathbf{K} = \begin{pmatrix} 0 & 0 & 0 \\ 0 & \dfrac{\boldsymbol{\sigma_u}}{\rho_0} & 0 \\ 0 & 0 & -\dfrac{\sigma_\theta}{\rho_0 c_v} \end{pmatrix} \tag{B5}$$

with $\sigma_{\mathbf{u}}$ a 3×3 matrix whose components are linear operators, to be determined as yet. Enforcement of the fluctuation-dissipation balance will allow to identify the linear operators, $\boldsymbol{\sigma_u}$ and σ_θ, appearing in Eq. (B5).

The system of equations (B1) can be linearized around the mean solution $\{\rho_0, \mathbf{0}, \theta_0\}$,

$$\partial_t \boldsymbol{\Delta} = \mathbf{L}\boldsymbol{\Delta} + \mathbf{f}, \tag{B6}$$

where $\mathbf{L}$ is the linearized Navier-Stokes operator with capillarity

$$\mathbf{L} = \begin{pmatrix} 0 & -\rho_0 \boldsymbol{\nabla}\cdot & 0 \\ -\dfrac{c_T^2}{\rho_0}\boldsymbol{\nabla} + \lambda \boldsymbol{\nabla}\boldsymbol{\nabla}^2 & \dfrac{\mu}{\rho_0}\left(\boldsymbol{\nabla}^2 + \dfrac{1}{3}\boldsymbol{\nabla}\boldsymbol{\nabla}\cdot\right) & -\dfrac{1}{\rho_0}\partial_\theta p \boldsymbol{\nabla} \\ 0 & -\dfrac{\theta_0}{\rho_0 c_v}\partial_\theta p \boldsymbol{\nabla}\cdot & \dfrac{k}{\rho_0 c_v}\boldsymbol{\nabla}^2 \end{pmatrix}, \tag{B7}$$

and $\boldsymbol{\Delta} = \{\delta\rho, \delta\mathbf{u}, \delta\theta\}$ the vector of fields fluctuations. Please notice that the energy equation has been rearranged in terms of temperature evolution to make it simpler to manage. Such linearization provides a set of stochastic partial differential equations, whose equilibrium (statistically stationary) solution is a set of Gaussian fields.

The solution of Eq. (B6) is formally expressed as [43]

$$\boldsymbol{\Delta}(x,t) = \int_0^t e^{\mathbf{L}(t-s)}\mathbf{f}(s)\, ds + e^{\mathbf{L}t}\boldsymbol{\Delta}_{\mathbf{0}}, \tag{B8}$$

where the last term which keeps memory of the initial conditions vanishes for large times. Consequently the equilibrium correlation is

$$\langle \boldsymbol{\Delta}(\tilde{x},t) \otimes \boldsymbol{\Delta}^{\dagger}(\hat{x},t) \rangle = \int_0^t e^{\mathbf{L}(t-s)}\mathbf{Q}\, e^{\mathbf{L}^{\dagger}(t-s)}\, ds, \tag{B9}$$

where $\mathbf{Q}$ was introduced in Eq. (B2) above. The above integral can be performed in closed form assuming the existence of a Hermitian nonsingular operator $\mathbf{E}^{-1}$ such that the operator $\mathbf{Q}$ can be decomposed as

$$\mathbf{Q} = -\mathbf{L}\mathbf{E}^{-1} - \mathbf{E}^{-1}\mathbf{L}^{\dagger}. \tag{B10}$$

With this position the integrand appearing in Eq. (B9) is the exact derivative with respect to the delay time s of $e^{\mathbf{L}(t-s)}\mathbf{E}^{-1}\,e^{\mathbf{L}^\dagger(t-s)}$. Hence Eq. (B9) leads to

$$\lim_{t\to\infty}\langle \mathbf{\Delta}\otimes\mathbf{\Delta}^\dagger\rangle = \mathbf{E}^{-1} = \mathbf{C}_{\mathbf{\Delta}}, \tag{B11}$$

and the operator $\mathbf{E}^{-1}$ exists indeed and coincides with the correlation matrix $\mathbf{C}_{\mathbf{\Delta}}$, defined in Eq. (13).

Given the expression for $\mathbf{Q}$, Eq. (B10), and the identity $\mathbf{E}^{-1} = \mathbf{C}_{\mathbf{\Delta}}$, it follows

$$\mathbf{Q} = -(\mathbf{L}\mathbf{C}_{\mathbf{\Delta}} + \mathbf{C}_{\mathbf{\Delta}}\mathbf{L}^\dagger) = (\mathbf{M}+\mathbf{M}^\dagger) = 2\mathrm{k}_B\mathbf{O}, \tag{B12}$$

where $\mathbf{M} = -\mathbf{L}\mathbf{C}_{\mathbf{\Delta}}$ and $\mathbf{O}$ can be recognized as the Onsager matrix. Relationship (B12) is the form the celebrated fluctuation-dissipation balance takes for the present system.

The unknown operators $\boldsymbol{\sigma_u}$ and σ_θ can be finally identified by substituting Eq. (B3) in Eq. (B2) and applying the FDB, Eq. (B12),

$$\mathbf{Q}(\tilde{x},\hat{x})\delta(t-t') = \mathbf{K}\langle\mathbf{W}\mathbf{W}^\dagger\rangle\mathbf{K}^\dagger = 2\mathrm{k}_B\mathbf{O}\delta(t-t'), \tag{B13}$$

hence

$$\mathbf{K}\mathbf{K}^\dagger = 2\mathrm{k}_B\mathbf{O} = -(\mathbf{L}\mathbf{C}_{\mathbf{\Delta}} + \mathbf{C}_{\mathbf{\Delta}}\mathbf{L}^\dagger) = \mathbf{M}+\mathbf{M}^\dagger. \tag{B14}$$

The matrix $\mathbf{M}$ can be obtained by substituting the expression for $\mathbf{L}$ given in Eq. (B7), and for the correlation matrix $\mathbf{C}_{\mathbf{\Delta}}$ from Eq. (13), resulting in

$$\mathbf{M} = \begin{pmatrix} 0 & m_{12} & 0 \\ m_{21} & \mathbf{m}_{22} & m_{23} \\ 0 & m_{32} & m_{33} \end{pmatrix}, \tag{B15}$$

whose entries are

$$m_{12} = m_{21} = \mathrm{k}_B\theta_0\nabla\delta(\mathbf{x}-\hat{\mathbf{x}}), \tag{B16}$$

$$m_{23} = m_{32} = \frac{\mathrm{k}_B\theta_0^2}{\rho_0^2 c_v}\partial_\theta p\nabla\delta(\mathbf{x}-\hat{\mathbf{x}}), \tag{B17}$$

$$\mathbf{m}_{22} = -\frac{\mu_0\mathrm{k}_B\theta_0}{\rho_0^2}\left(\mathbf{I}\nabla^2 + \frac{1}{3}\nabla\otimes\nabla\right)\delta(\mathbf{x}-\hat{\mathbf{x}}), \tag{B18}$$

$$m_{33} = -\frac{\mathrm{k}_B\theta_0^2 k}{\rho_0^2 c_v^2}\nabla^2\delta(\mathbf{x}-\hat{\mathbf{x}}). \tag{B19}$$

Thus, the sum of $\mathbf{M}$ with its hermitian conjugate $\mathbf{M}^\dagger$ provides

$$\mathbf{M}+\mathbf{M}^\dagger = \mathbf{K}\mathbf{K}^\dagger = \begin{pmatrix} 0 & 0 & 0 \\ 0 & 2\mathbf{m}_{22} & 0 \\ 0 & 0 & 2m_{33} \end{pmatrix}. \tag{B20}$$

In order to find an expression for $\mathbf{K}$ consistent with the FDB, the system of equations (B20) must be satisfied component-wise, so that

$$\sigma_\theta\sigma_\theta^\dagger = -2\mathrm{k}_B\theta_0^2 k\nabla^2\delta(\hat{\mathbf{x}}-\tilde{\mathbf{x}}), \tag{B21}$$

$$\sigma_{\mathbf{u}}\otimes\sigma_{\mathbf{u}}^\dagger = -2\mu_0\mathrm{k}_B\theta_0\left(\mathbf{I}\nabla^2 + \frac{1}{3}\nabla\otimes\nabla\right)\delta(\hat{\mathbf{x}}-\tilde{\mathbf{x}}), \tag{B22}$$

providing an explicit expression for the stochastic fluxes

$$\boldsymbol{\delta\Sigma} = \sqrt{2\mu_0\mathrm{k}_B\theta_0}\tilde{\mathbf{W}}_{\mathbf{u}} - \frac{1}{3}\sqrt{2\mu\mathrm{k}_B\theta}\,\mathrm{Tr}(\tilde{\mathbf{W}}_{\mathbf{u}})\mathbf{I}, \tag{B23}$$

$$\boldsymbol{\delta q} = \sqrt{2k\mathrm{k}_B\theta_0^2}\mathbf{W}_\theta. \tag{B24}$$

In Eq. (B23), $\tilde{\mathbf{W}}_{\mathbf{u}} = [\mathbf{W}_{\mathbf{u}} + (\mathbf{W}_{\mathbf{u}})^T]/\sqrt{2}$ is a stochastic symmetric tensor field, and $\mathbf{W}_\theta$ is a stochastic vector, with the following statistical properties:

$$\left\langle {W^u}_{\alpha\beta}(\hat{x},\hat{t}) {W^u}_{\gamma\delta}(\tilde{x},\tilde{t}) \right\rangle = \delta_{\alpha\gamma}\delta_{\beta\delta}\delta(\hat{x}-\tilde{x})\delta(\hat{t}-\tilde{t}), \tag{B25}$$

$$\left\langle {W^\theta}_{\alpha}(\hat{x},\hat{t}) {W^\theta}_{\beta}(\tilde{x},\tilde{t}) \right\rangle = \delta_{\alpha\beta}\delta(\hat{x}-\tilde{x})\delta(\hat{t}-\tilde{t}). \tag{B26}$$

It is straightforward to show that expressions (B23) and (B24) are consistent with Eqs. (B21) and (B22), in fact,

$$\langle \sigma_\theta W_\theta W_\theta^\dagger \sigma_\theta^\dagger \rangle = \langle \nabla_{\hat{\mathbf{x}}} \cdot \boldsymbol{\delta q}(\hat{\mathbf{x}},t) \nabla_{\tilde{\mathbf{x}}} \cdot \boldsymbol{\delta q}(\tilde{\mathbf{x}},t) \rangle = -2\mathrm{k}_B\theta_0^2 k \nabla^2 \delta(\hat{\mathbf{x}}-\tilde{\mathbf{x}}), \tag{B27}$$

$$\langle \boldsymbol{\sigma}_{\boldsymbol{u}} \mathbf{W}_{\mathbf{u}} \otimes \mathbf{W}_{\mathbf{u}}{}^\dagger \boldsymbol{\sigma}_{\boldsymbol{u}}^\dagger \rangle = \langle \nabla_{\hat{\mathbf{x}}} \cdot \boldsymbol{\delta\Sigma}(\hat{\mathbf{x}},t) \otimes \nabla_{\tilde{\mathbf{x}}} \cdot \boldsymbol{\delta\Sigma}(\tilde{\mathbf{x}},t) \rangle = -2\mu_0 \mathrm{k}_B\theta_0 \left(\mathbf{I}\nabla^2 + \frac{1}{3}\nabla\otimes\nabla \right) \delta(\hat{\mathbf{x}}-\tilde{\mathbf{x}}). \tag{B28}$$

Moreover, by means of the FDB, the covariance of the stochastic process reads

$$\langle \boldsymbol{\delta\Sigma}(\hat{x},\hat{t}) \otimes \boldsymbol{\delta\Sigma}^\dagger(\tilde{x},\tilde{t}) \rangle = \mathbf{Q}^\Sigma \delta(\hat{x}-\tilde{x})\delta(\hat{t}-\tilde{t}), \tag{B29}$$

with

$${\mathbf{Q}^\Sigma}_{\alpha\beta\nu\eta} = 2\mathrm{k}_B\theta\mu\left(\delta_{\alpha\nu}\delta_{\beta\eta} + \delta_{\alpha\eta}\delta_{\beta\nu} - \tfrac{2}{3}\delta_{\alpha\beta}\delta_{\nu\eta}\right), \tag{B30}$$

and

$$\langle \boldsymbol{\delta q}(\hat{x},\hat{t}) \otimes \boldsymbol{\delta q}^\dagger(\tilde{x},\tilde{t}) \rangle = \mathbf{Q}^{\mathbf{q}} \delta(\hat{x}-\tilde{x})\delta(\hat{t}-\tilde{t}), \tag{B31}$$

with

$${\mathbf{Q}^{\mathbf{q}}}_{\alpha\beta} = 2\mathrm{k}_B\theta^2 k \delta_{\alpha\beta}. \tag{B32}$$

[1] F. Detcheverry and L. Bocquet, Thermal Fluctuations in Nanofluidic Transport, Phys. Rev. Lett. **109**, 024501 (2012).

[2] L. Bocquet and E. Charlaix, Nanofluidics, from bulk to interfaces, Chem. Soc. Rev. **39**, 1073 (2010).

[3] A. Naji, P. J. Atzberger, and F. L. H. Brown, Hybrid Elastic and Discrete-Particle Approach to Biomembrane Dynamics with Application to the Mobility of Curved Integral Membrane Proteins, Phys. Rev. Lett. **102**, 138102 (2009).

[4] C. S. Peskin, G. M. Odell, and G. F. Oster, Cellular motions and thermal fluctuations: The Brownian ratchet, Biophys. J. **65**, 316 (1993).

[5] C. E. Brennen, *Cavitation and Bubble Dynamics* (Cambridge University Press, Cambridge, 2013).

[6] L. Cao, A. K. Jones, V. K. Sikka, J. Wu, and D. Gao, Anti-icing superhydrophobic coatings, Langmuir **25**, 12444 (2009).

[7] S. F. Jones, G. M. Evans, and K. P. Galvin, Bubble nucleation from gas cavities — a review, Adv. Colloid Interface Sci. **80**, 27 (1999).

[8] D. Kashchiev and G. M. Van Rosmalen, Review: Nucleation in solutions revisited, Cryst. Res. Technol. **38**, 555 (2003).

[9] D. Lohse and A. Prosperetti, Homogeneous nucleation: Patching the way from the macroscopic to the nanoscopic description, Proc. Natl. Acad. Sci. USA **113**, 13549 (2016).

[10] M. Blander and J. L. Katz, Bubble nucleation in liquids, AIChE J. **21**, 833 (1975).

[11] D. W. Oxtoby and R. Evans, Nonclassical nucleation theory for the gas-liquid transition, J. Chem. Phys. **89**, 7521 (1988).

[12] J. F. Lutsko, Density functional theory of inhomogeneous liquids. IV. Squared-gradient approximation and classical nucleation theory, J. Chem. Phys. **134**, 164501 (2011).
[13] J. Diemand, R. Angélil, K. K. Tanaka, and H. Tanaka, Direct simulations of homogeneous bubble nucleation: Agreement with classical nucleation theory and no local hot spots, Phys. Rev. E **90**, 052407 (2014).
[14] E. Weinan, W. Ren, and E. Vanden-Eijnden, String method for the study of rare events, Phys. Rev. B **66**, 052301 (2002).
[15] R. J. Allen, C. Valeriani, and P. R. ten Wolde, Forward flux sampling for rare event simulations, J. Phys.: Condens. Matter **21**, 463102 (2009).
[16] P. G. Bolhuis, D. Chandler, C. Dellago, and P. L. Geissler, Transition path sampling: Throwing ropes over rough mountain passes, in the dark, Annu. Rev. Phys. Chem. **53**, 291 (2002).
[17] A. Giacomello, S. Meloni, M. Chinappi, and C. M. Casciola, Cassie-Baxter and Wenzel states on a nanostructured surface: Phase diagram, metastabilities, and transition mechanism by atomistic free energy calculations, Langmuir **28**, 10764 (2012).
[18] L. D. Landau and E. M. Lifshitz, *Course of Theoretical Physics*, Vol. 5, part I, 3rd ed. (Pergamon International Library, Hoddesdon, UK, 1980).
[19] R. F. Fox and G. E. Uhlenbeck, Contributions to non-equilibrium thermodynamics. I. Theory of hydrodynamical fluctuations, Phys. Fluids **13**, 1893 (1970).
[20] A. Donev, E. Vanden-Eijnden, A. Garcia, and J. Bell, On the accuracy of finite-volume schemes for fluctuating hydrodynamics, Comm. Appl. Math. Comput. Sci. **5**, 149 (2010).
[21] S. Delong, B. E. Griffith, E. Vanden-Eijnden, and A. Donev, Temporal integrators for fluctuating hydrodynamics, Phys. Rev. E **87**, 033302 (2013).
[22] F. Balboa, J. B. Bell, R. Delgado-Buscalioni, A. Donev, T. G. Fai, B. E. Griffith, and C. S. Peskin, Staggered schemes for fluctuating hydrodynamics, Multiscale Model. Simul. **10**, 1369 (2012).
[23] A. Donev, A. Nonaka, Y. Sun, T. Fai, A. Garcia, and J. Bell, Low Mach number fluctuating hydrodynamics of diffusively mixing fluids, Comm. Appl. Math. Comput. Sci. **9**, 47 (2014).
[24] J. D. Van der Waals, The thermodynamic theory of capillarity under the hypothesis of a continuous variation of density, J. Stat. Phys. **20**, 200 (1979).
[25] F. Magaletti, L. Marino, and C. M. Casciola, Shock wave formation in the collapse of a vapor nanobubble, Phys. Rev. Lett. **114**, 064501 (2015).
[26] A. Chaudhri, J. B. Bell, A. L. Garcia, and A. Donev, Modeling multiphase flow using fluctuating hydrodynamics, Phys. Rev. E **90**, 033014 (2014).
[27] R. Angélil, J. Diemand, K. K. Tanaka, and H. Tanaka, Bubble evolution and properties in homogeneous nucleation simulations, Phys. Rev. E **90**, 063301 (2014).
[28] E. Weinan, W. Ren, and E. Vanden-Eijnden, Simplified and improved string method for computing the minimum energy paths in barrier-crossing events, J. Chem. Phys. **126**, 164103 (2007).
[29] F. Magaletti, M. Gallo, L. Marino, and C. M. Casciola, Shock-induced collapse of a vapor nanobubble near solid boundaries, Int. J. Multiphase Flow **84**, 34 (2016).
[30] J. K. Johnson, J. A. Zollweg, and K. E. Gubbins, The Lennard-Jones equation of state revisited, Mol. Phys. **78**, 591 (1993).
[31] https://www.nist.gov/mml/csd/chemical-informatics-research-group/lennard-jones-fluid-properties.
[32] F. Dell'Isola, H. Gouin, and G. Rotoli, Nucleation of spherical shell-like interfaces by second gradient theory: Numerical simulations, Eur. J. Mech. B Fluids **15**, 545 (1996).
[33] J. W. Cahn and J. E. Hilliard, Free energy of a nonuniform system. III. Nucleation in a two-component incompressible fluid, J. Chem. Phys. **31**, 688 (1959).
[34] S. R. De Groot and P. Mazur, *Non-Equilibrium Thermodynamics* (Courier Dover Publications, New York, 2013).
[35] D. Jamet, O. Lebaigue, N. Coutris, and J. M. Delhaye, The second gradient method for the direct numerical simulation of liquid-vapor flows with phase change, J. Comput. Phys. **169**, 624 (2001).
[36] J. M. O. De Zarate and J. V. Sengers, *Hydrodynamic Fluctuations in Fluids and Fluid Mixtures* (Elsevier, Amsterdam, 2006).

[37] P. J. Atzberger, Spatially adaptive stochastic numerical methods for intrinsic fluctuations in reaction-diffusion systems, J. Comput. Phys. **229**, 3474 (2010).
[38] J. Kestin, J. V. Sengers, B. Kamgar-Parsi, and J. M. H. L. Sengers, Thermophysical properties of fluid H_2O, J. Phys. Chem. Ref. Data **13**, 175 (1984).
[39] See Supplemental Material at http://link.aps.org/supplemental/10.1103/PhysRevFluids.3.053604 for details.
[40] S.-I. Tsuda, S. Takagi, and Y. Matsumoto, A study on the growth of cavitation bubble nuclei using large-scale molecular dynamics simulations, Fluid Dyn. Res. **40**, 606 (2008).
[41] B. R. Novak, E. J. Maginn, and M. J. McCready, Comparison of heterogeneous and homogeneous bubble nucleation using molecular simulations, Phys. Rev. B **75**, 085413 (2007).
[42] R. L. Stratonovich, *Nonlinear Nonequilibrium Thermodynamics I: Linear and Nonlinear Fluctuation-Dissipation Theorems* (Springer Science and Business Media, New York, 2012), Vol. 57.
[43] G. Da Prato, *Kolmogorov Equations for Stochastic PDEs* (Birkhäuser, Basel, 2012).